2002ESASP.487..689E

QUALIFICATION OF HEAT FLUX SENSORS IN HIGH ENTHALPY FLOWS

B. Esser, A. Gülhan, U. Koch
DLR, Institute of Aerodynamics and Flow Technology, Windtunnel Section Köln-Porz
Linder Höhe, 51170 Köln, Germany
Phone: (49) 2203 601 2198
Fax: (49) 2203 601 2344
e-Mail: Burkard.Esser@dlr.de

ABSTRACT

Comparative heat flux measurements were performed in the hypersonic high enthalpy flow field of the arc heated facility L2K. Three different sensors were compared: two cold wall heat flux sensors, a heat flux microsensor and a transient probe, and one hot wall heat flux sensor, which is made of tile material and is applicable at surface temperatures up to 1500 K. Tests were carried out in both, stagnation point and flat plate configuration at two flow conditions with different specific enthalpies. For the stagnation point tests the influence of model and sensor geometry was excluded by integrating the sensors into a flat faced cylinder with a diameter of 100 mm. In flat plate configuration the sensors were embedded in an insulation material to avoid heat conduction to the water-cooled model holder. Furthermore, flat plate testing was used to investigate the sensors' sensitivity to extraneous radiation, which emanates from the reservoir of high enthalpy facilities or hot surfaces of re-entry vehicles. The results confirm that extraneous radiation has an influence on the measurement and has to be considered in the evaluation of measured data.

1. INTRODUCTION

Intrusive measurement techniques in supersonic and hypersonic flows have been a challenging task for engineers for decades. Recent progresses in non-intrusive measurement techniques and numerical codes have led to a better understanding of local flow phenomena and to further improvement of intrusive measurement techniques in aerodynamics. Because of its complexity the measurement of heat flux rates remains one of the key techniques, which has to be improved with respect to accuracy and repeatability. Usually, the heat flux rate is determined from temperature histories, which are measured on the surface or inside a probe, by applying a mathematical model with some, in most cases simplifying assumptions. Any deviation from a perfect contact between temperature sensor and probe as well as any other mal-satisfaction of the assumptions leads to inaccuracies in the heat flux data.

Heat flux determination in high enthalpy flow fields is accompanied with additional effects. The flow field of most high enthalpy facilities is in thermo-chemical non-equilibrium and gas-surface interaction phenomena influence the heat flux rate significantly. Surface catalysis and emittance, which are a function of the surface temperature, play an important role in such environments. The boundary flow around the probe is also influenced by these effects and there is a continuous coupling between flow and model structure.

Due to differences in facility operation there are different requirements on heat flux sensors for the different kinds of high enthalpy facilities. Short duration facilities like shock tunnels, impulse facilities, etc. have a very short testing time in the order of several milliseconds. Therefore only heat flux sensors with a very short response time can be used in these facilities. The sensor is exposed to the flow for a short time only, and the surface temperature keeps low. Arc heated and induction heated facilities have a much longer testing time and allow long duration measurements. Here the influences of probe cooling and insulation have to be considered carefully, since most of the sensors are limited with respect to surface temperature. Another option is the application of uncooled transient heat flux probes, whose reliability depends on further parameters like sweep speed, flow homogeneity, etc. For applications at surface temperatures beyond 1300 K heat flux sensors made of tile material are used. Such sensors are expensive and require more complex data reduction procedures, but they are unique in terms of providing accurate data at high temperatures.

2. HEAT FLUX PROBES

Different types of heat flux sensors were compared during tests in the arc heated facility LBK. The set of sensors included two cold wall heat flux sensors, i.e. a transient heat flux probe and a so-called "heat flux microsensor" (HFM), and one hot wall heat flux sensor made of tile material.

2.1 Transient Heat Flux Probe

The transient heat flux probe consists of a copper cylinder with two embedded thermocouples at both ends [1]. It is integrated almost adiabatically in a water cooled probe holder. For measurement the probe is swept through the flow field. Since the probe's surface temperature usually remains below 500 K and its copper

---

Proc. 4th Europn Symp. Aerothermodynamics for Space Applications, 15-18 Oct. 2001, Capua, Italy, ESA SP-487, March 2002

© European Space Agency • Provided by the NASA Astrophysics Data System

surface is almost fully catalytic, it provides cold wall heat flux rates to a catalytic surface. The heat flux rate is evaluated from the temperature histories, which are measured with the two thermocouples. These temperatures are prescribed as boundary conditions to a one-dimensional heat conduction analysis. Temperature dependency of the material properties is taken into account in order to achieve a better accuracy. The analysis is based on the assumption that no heat is lost to the thermocouple wires or by conduction radial in direction. The main advantage of this technique is that it allows to measure the spatial distribution of the heat flux rate across the flow field. Its major technical uncertainty is correlated to the quality of vacuum brazing the thermocouples into the copper cylinder.

2.2 Heat Flux Microsensor (HFM)

The heat flux microsensor HFM consists of two elements: a thermopile heat flux sensor HFS and a resistance temperature sensing element RTS [2]. The RTS is composed of a pure platinum thin film, which is deposited in a loop pattern around the outer edge of the sensor's face. The HFS consists of several thin-film layers forming a differential thermopile across a thermal resistance layer of aluminum nitride. Since this layer is very thin ($\delta \approx 1$ µm), the temperature difference across the layer is extremely small, even at high heat fluxes. Therefore, many thermocouple pairs are put in series to form a differential thermopile, which gives a measurable signal even at low heat flux rates. Platinum and Nichrome are used as thermocouple material, since they have a large thermoelectric potential and can withstand temperatures up to 1000 K. The response time of the heat flux sensor (HFS) is about 6 µs. HFS allows to measure both, transient and steady components of the heat flux rate. The RTS signal is used for correction of the HFS signal with respect to the sensor's surface temperature. The surface of the HFM sensor is coated with a thin Zynolyte layer to reach a high surface emissivity value of 0.94 in the spectral range around 2 µm.

2.3 Tile Heat Flux Sensor

In order to measure heat flux rates at surface temperatures up to 1623 K, a high temperature heat flux sensor made of tile material was developed by Kawasaki Heavy Ind. (KHI) [3]. The sensor consists of a cylindrical block made of tile material with five embedded thermocouples and a thin black glass coating. It has a diameter of 100 mm and a length of 50 mm. The edges of the front surface have a radius of 5 mm. Three thermocouples are integrated nearly along the center axis of the sensor (Fig. 1). The first thermocouple TC1 is placed directly below the glass coating, which has a thickness of 300 µm. TC2 and TC3 are located 22.6 mm and 44.7 mm below the front surface, respectively. Common thermal analysis codes can be used for the determination of heat fluxes. Besides information about geometry and material properties only the measured data of TC1 and TC3 are required for the analysis. The other thermocouples have a control function. TC4, which is placed at 25 mm off-axis position, allows to check the heat flux homogeneity across the sensor's surface. TC5 is integrated in the side wall at nearly the same height as TC2, and can be used to estimate the influence of lateral heat flux through the side surface.

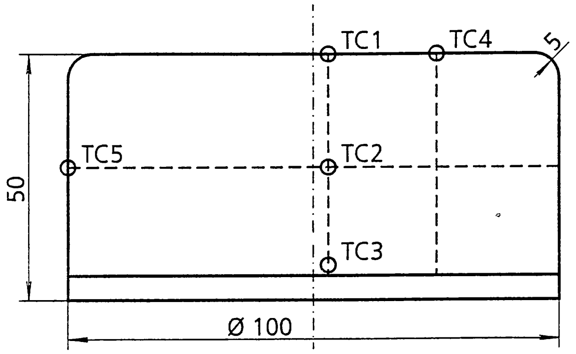

Figure 1. Thermocouple configuration of the tile sensor.

A one-dimensional thermal model consisting of 46 solid elements was used for the computation of heat flux rates. The model takes into account that most of the tile material's properties are functions of the temperature and that its thermal conductivity furthermore depends on the pressure. In all computations the measured history of TC1 was prescribed as a boundary condition at the front surface. On the rear side boundary three different boundary conditions (measured history of TC3, adiabatic and semi-infinite wall) were applied, and it was found that the heat fluxes at the front surface as well as the temperatures inside the sensor are almost non-sensitive to this rear boundary condition.

2.4 Model Geometry

For the tests in stagnation point configuration, HFM sensor and transient probe were integrated in a flat faced cylinder, which has an outer shape which is identical to the shape of the tile sensor. This was done in order to exclude the influence of the model geometry, i.e. shock stand-off distance and shock shape, on the heat flux rate. The variation of the model geometry was subject of a separate study [4]. In flat plate configuration the sensors were embedded in an insulation material to avoid heat conduction to the water-cooled model holder.

3. FLOW CHARACTERIZATION

All tests were carried out in the 1 MW test leg L2K of the arc heated facility LBK [5]. To analyze the differences between the sensors with respect to surface catalysis

© European Space Agency • Provided by the NASA Astrophysics Data System

2002ESASP.487..689E

and the influence of radiation, tests were performed at two test conditions (FC I and FC II) with different enthalpy levels. A conical nozzle with a 29 mm throat diameter, 12° half angle and 200 mm exit diameter was used. The model was positioned 200 mm and 555 mm behind the nozzle exit for flow conditions FC I and FC II, respectively.

From air mass flow rate and reservoir pressure, which were continuously measured during the tests, all other gas parameters were calculated using the NATA code, which is a quasi one-dimensional flow solver including non-equilibrium chemistry [6]. The results are listed in Table 1. For the high enthalpy flow condition FC II, the molecular oxygen is almost fully dissociated and the concentration of NO is negligible. The aggressive atomic oxygen reaches a concentration level of 34%. At the lower specific enthalpy of FC I the oxygen is only partly dissociated leaving a concentration of 5% for oxygen molecules. For this test condition gas parameters measured by applying sophisticated spectroscopic techniques are available [7,8]. In addition to the computations the Pitot pressure was measured using a water cooled probe. The measured values of 11.8 hPa (FC I) and 23.5 hPa (FC II) are in good agreement with the computed data.

Table 1. Flow parameters of the test conditions.

Flow condition	FC I	FC II
air mass flow rate, $\dot{m}$ [g/s]	49	36
reservoir pressure, p_0 [hPa]	1300	1100
reservoir temperature, T_0 [K]	3907	4935
specific enthalpy, h_0 [MJ/kg]	7.3	10.1
model position from nozzle throat, x_t [mm]	972	607
model position from nozzle exit, x_e [mm]	550	200
free stream temperature, T_∞ [K]	340	586
free stream pressure, p_∞ [hPa]	0.160	0.425
free stream density, ρ_∞ [kg/m^3]	$1.4 \cdot 10^{-4}$	$2.1 \cdot 10^{-4}$
Pitot pressure, p_{t2} [hPa]	12.2	22.9
mole fraction of O2, n_{O_2} [-]	0.05	$1.8 \cdot 10^{-3}$
mole fraction of O, n_O [-]	0.231	0.341
mole fraction of N2, n_{N_2} [-]	0.676	0.650
mole fraction of N, n_N [-]	$5 \cdot 10^{-8}$	$9.5 \cdot 10^{-4}$
mole fraction of NO, n_{NO} [-]	0.043	$6 \cdot 10^{-3}$
mole fraction of NO$^+$, n_{NO^+} [-]	$1.7 \cdot 10^{-7}$	$5.9 \cdot 10^{-7}$

Flow homogeneity was verified by measuring radial Pitot pressure and heat flux profiles at both flow conditions. The heat flux profile was measured with the transient probe, which had been integrated in a cylinder with a diameter of 50 mm and an edge radius of 11.5 mm for this measurement.

The profiles measured at FC I are plotted in Fig. 2. Both, pressure and heat flux measurements provide a similar profile and show a homogeneous flow core of around 120 mm. Since the measurements were taken far downstream of the nozzle exit at 555 mm, the size of the homogeneous core is influenced by expansion waves, which are induced at the interface between nozzle exit and test chamber due to under-expanded nozzle operation and then propagate toward the nozzle axis.

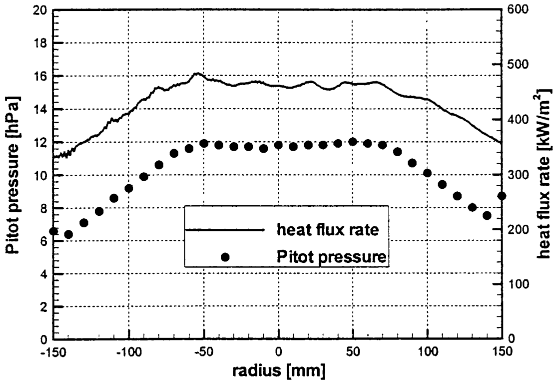

Figure 2. **Measured Pitot pressure and heat flux profiles at FC I.**

At FC II the specific enthalpy is higher and the model is closer to the nozzle exit (200 mm). This leads to higher Pitot pressures and heat flux rates (Fig. 3). An excellent agreement was noticed between two measurement series of the Pitot pressure. Both profiles confirm a homogeneous flow core of about 160 mm at this flow condition, which is in coincidence with former experimental and numerical studies [9].

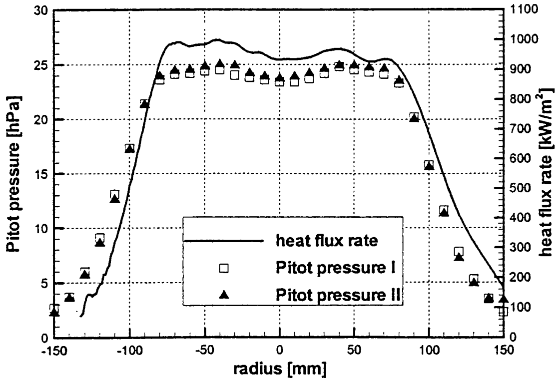

Figure 3. **Measured Pitot pressure and heat flux profiles at FC II.**

© European Space Agency • Provided by the NASA Astrophysics Data System

2002ESASP.487..689E

4. HEAT FLUX MEASUREMENTS

In order to cover a broad range of heat flux rates, tests were performed in stagnation point and flat plate configuration. During arc heater ignition all sensors were positioned outside the flow field and remained there, until steady state flow conditions were achieved. Afterwards the sensors were moved into the flow field for the measurement. Steady state condition was checked by monitoring air mass flow rate and reservoir pressure.

4.1 Stagnation Point Configuration

Figure 4 shows the tile sensor mounted on the model holder in the hypersonic high enthalpy flow field at flow condition FC I. In addition to the thermocouples TC1 and TC4 two pyrometers, a spectral pyrometer P1 and a two-color pyrometer P2, were used for the measurement of the sensor's surface temperature. Both were adjusted to the location of TC1. An emissivity value of 0.88 was used for pyrometer P1.

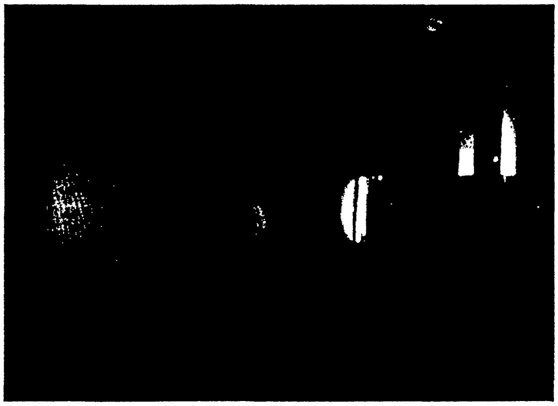

Figure 4. Tile sensor in the high enthalpy flow.

The measured surface temperature and the temperature development inside the sensor are plotted in Fig. 5. Both, the spectral pyrometer P1 and the two-color pyrometer P2 have a measurement range between 1173 K and 3273 K and provide a constant signal of 1173 K for any temperature below. The good agreement between the final surface temperatures measured with P1 (1413 K) and P2 (1417 K) indicates a grey-surface behavior of the black glass coating in the spectral range of the pyrometers (around 1 µm). The temperature measured with TC1 behind the surface coating is 30 K lower than the value indicated by P1. The heat conduction through this thin coating and the adhesive material between coating and thermocouple is responsible for this small difference. The data of TC1 and TC4 agree very well, which confirms flow homogeneity, i.e. a uniform heat flux distribution across the sensor's surface.

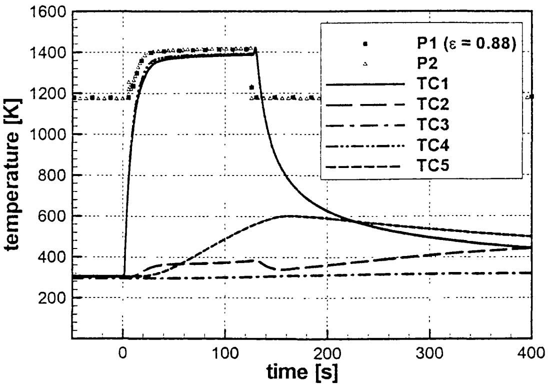

Figure 5. Temperatures measured with the tile sensor in the stagnation point test at FC I.

For the stagnation point test at FC I the computed heat fluxes at the sensor surface are plotted in Fig. 6. The highest heat conduction into the model is observed immediately after the model injection into the flow. At that time the surface temperature is still low, so there is a large difference between gas and surface temperature combined with a low level of surface radiation. With time and increasing surface temperature the radiation losses increase according to the Stefan-Boltzmann law. But after 120 s, at the end of the hot test phase, radiative equilibrium has not yet established on the surface. The conductive heat flux still amounts to 5% of the convective heat flux at that time. So assuming a radiative equilibrium, which means neglecting the heat conduction, would provide a 5% failure in the heat flux rate.

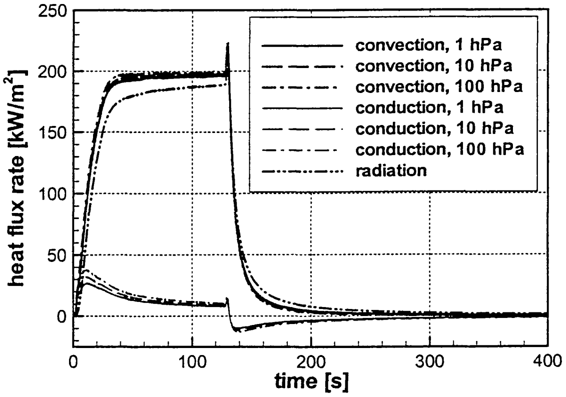

Figure 6. Computed heat flux rates for the stagnation point test at FC I.

As mentioned before, the analysis includes the pressure and temperature dependency of the tile material's properties. The influence of the ambient pressure on the thermal conductivity cannot be neglected, which is confirmed by the fact that for the three pressure levels of 1 hPa, 10 hPa and 100 hPa different heat flux rates are obtained. Since the convective heating is the sum of the heat conduction and radiation, it also depends on the

© European Space Agency • Provided by the NASA Astrophysics Data System

2002ESASP.487..689E

pressure level. The radiative heat flux, however, is calculated from the measured surface temperature and therefore is not influenced by the pressure.

The reliability of the thermal analysis was verified by comparing measured and calculated temperature histories of TC2. Due to its position at mid-height on the axis of symmetry, the TC2 data are very useful for the verification and explanation of physical processes. Figure 7 shows the computed TC2 temperatures for different pressure levels in comparison with the measured data.

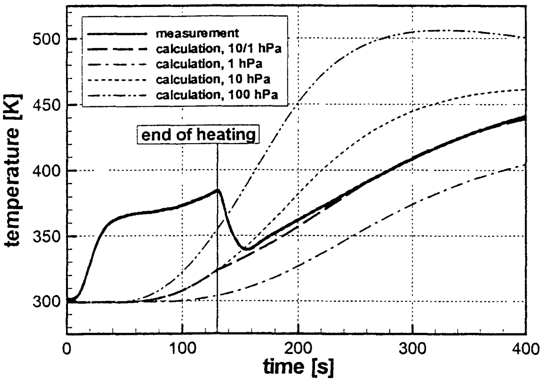

Figure 7. Calculated and measured TC2 temperatures for the stagnation point test at FC I.

During the hot test phase all calculated temperatures differ from the measured data remarkably. This is due to the complex integration geometry of TC2, which was not included in the thermal model, but causes the measured data to be influenced by internal convection and radiation processes during the hot test phase.

After the hot test phase, when there is no convective heating, the temperature history provides very useful data. There are 3 temperature histories plotted in Fig. 7, which are based on a pressure level of 1, 10 and 100 hPa, resp., being constant throughout the complete time period. For 10 and 100 hPa the calculated temperatures are much higher than the measured one. For a pressure level of 1 hPa the calculated temperatures are too low, but this curve shows after the end of heating the same tendency as the measured history. But the assumption of a constant pressure level for the complete calculation is very rough for the stagnation point configuration. An almost perfect match between measurement and computation after the hot phase is achieved, when the Pitot pressure, which is in the order of 10 hPa, is considered for the hot test phase, and the test chamber background pressure, which is slightly below 1 hPa, afterwards.

To achieve the same shock stand-off distance as ahead of the tile sensor, the microsensor HFM and the transient probe were integrated into a steel cylinder with the tile sensor's outer geometry. In order to keep the surface temperature safely below the upper limit of 1000 K, the testing time had to be reduced in comparison to the tests with the tile sensor. For the stagnation point configuration the sensor was moved into the flow, remained on the flow axis for about 3 seconds and was swept out afterwards.

The heat flux rates (q_g), which were measured with tile sensor, HFM, and transient probe at the two test conditions FC I and FC II, as well as the corresponding final surface temperatures (T_s) at the end of the hot testing phase are listed in Table 2.

Table 2. Heat flux rates measured in stagnation point configuration.

	FC I		FC II	
Sensor	$\dot{q}_g$ [kW/m^2]	T_s [K]	$\dot{q}_g$ [kW/m^2]	T_s [K]
Tile sensor	197±3	1417	245±4	1492
Heat flux microsensor	297±3	385	544±9	411
transient probe	272±11	413	555±21	463

At both flow conditions HFM sensor and transient probe indicate nearly the same heat fluxes. Due to the higher surface temperature the values are significantly lower for the tile sensor.

4.2 Flat Plate Configuration

The flat plate model holder consists of a water cooled metallic nose and base plate and two side plates (Fig. 8).

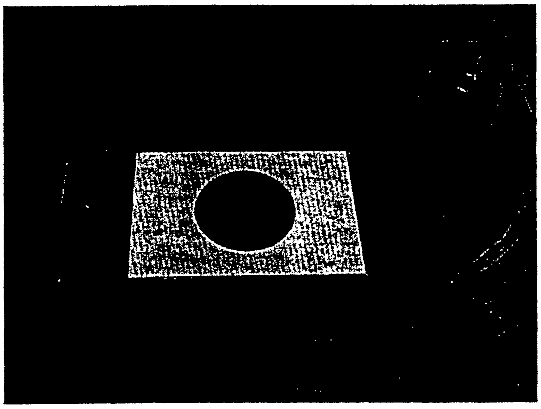

Figure 8. Flat plate holder with integrated tile sensor.

The sensor assembly, which has an outer diameter of 100 mm, was insulated from the water cooled holder using an insulation material based on alumina and silica. The insulation material is 144 mm wide and 170 mm

© European Space Agency • Provided by the NASA Astrophysics Data System

2002ESASP.487..689E

long with a height of nearly 60 mm. The total height of the holder is about 115 mm.

In addition to comparative heat flux measurements the flat plate configuration was also applied to determine the influence of the arc heater radiation on the measurements. This was done by moving the model to symmetrical off-axis positions, at which the influence of radiation either was completely blocked or it existed.

4.2.1 Measurement with the Tile Sensor

Figure 9 shows an IR image of the tile sensor assembly during a test at an angle of attack of 0°. The surface temperature distribution is very homogeneous in vertical direction, which is perpendicular to the flow. The image was taken for an emissivity value of 0.8, which is the emissivity of the sensor material in the spectral range of the IR-camera (7.5-12 μm). Since the surface emissivity of the insulation material is higher than 0.8 (around 0.95), the real surface temperature of the insulator is lower than indicated by the IR image. In addition, the surface catalysis is higher on the insulation material compared to the tile sensor, which leads to higher heat flux rates and surface temperatures there.

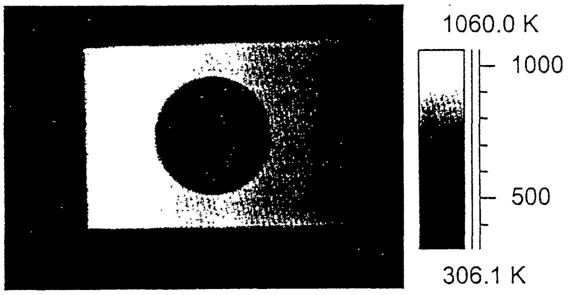

Figure 9. IR image of the tile sensor in the flat plate configuration (flow from left to right).

The temperature development, which was measured with the thermocouples of the tile sensor, is shown in Fig. 10.

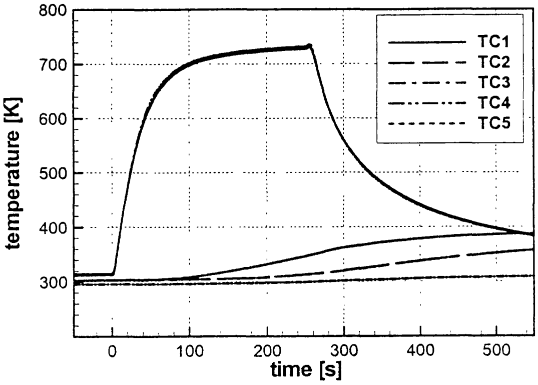

Figure 10. Temperatures measured with the tile sensor in flat plate configuration

Again, the agreement between thermocouples TC1 and TC4 is very good and indicates a homogeneous distribution of the heat flux rate across the sensor's surface. After 240 s, at the end of the hot test phase, TC1 measures a temperature of 730 K. At that time, the IR camera provides a temperature of 744 K for the surface spot above TC1. The difference of 14 K is in coincidence with the measurements in stagnation point configuration, where a temperature drop of 15-30 K over the black glass coating was observed by comparing the pyrometer data and TC1. Since in the flat plate configuration the surface temperature is remarkably lower, the temperature difference across the coating should also be smaller. So the data of the IR camera and TC1 indicate that the emissivity of the surface coating is very close to 0.8 in the spectral range of 7.5-12 μm.

Compared to the stagnation point tests the temperature increase at the locations of TC2, TC3 and TC5 was much lower during this test. With regard to the setup there is one major difference in this configuration, since the sensor's side surface is much better insulated. So, heat and hot gas penetration through side surface or rear part of the sensor, which had to be considered for the stagnation point setup, is almost completely blocked. As a consequence, the nearly stepwise increase and decrease of the TC2 reading, which had been observed during the hot phase of the stagnation point tests, is not observed here.

The heat flux rates, which were calculated from the measured temperature histories of TC1 and TC3 and the sensor's surface and material properties for two ambient pressure levels, are given in Fig. 11. The convective heat flux rate is nearly 16 kW/m^2. The difference between the convective and the radiative heat fluxes at the end of the hot test phase shows, that at this low heat flux level, even after more than 4 minutes, radiative equilibrium has not yet established.

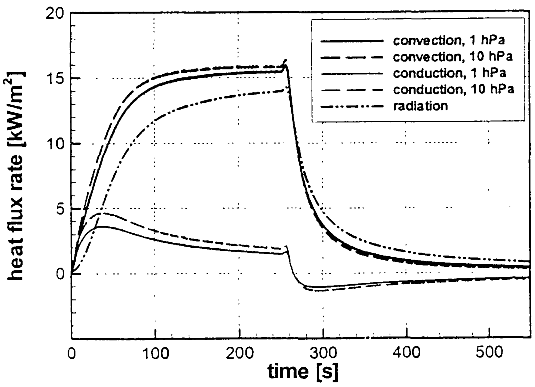

Figure 11. Computed heat flux rates for the tile sensor in flat plate configuration.

© European Space Agency • Provided by the NASA Astrophysics Data System

2002ESASP.487..689E

The histories of calculated and measured temperatures of TC2 fit very well, even during the hot test phase (Fig. 12).

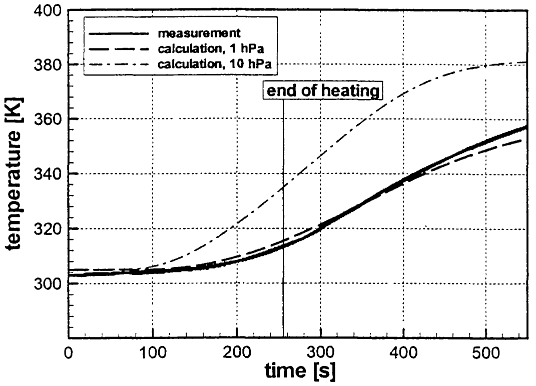

Figure 12. Measured and calculated TC2 temperatures for flat plate configuration.

In order to check, whether the arc heater radiation has an influence on the heat flux measurements with the tile sensor, a test with a modified test procedure was performed at FC I. The sensor was not positioned on the flow axis, but at distances of –20 mm and +20 mm off the axis. Because of the axial symmetry of the flow field, the free stream flow parameters as well as the convective heating to the surface are same for both positions. The sensor was first positioned at –20 mm, where the arc heater radiation is completely blocked from the sensor and the surface is heated by convection only. After a period of 235 s the sensor was moved to the +20 mm position, where its surface is partly exposed to the arc heater radiation. Owing to the arc heater radiation the convective heat flux rate to the tile sensor increases about 9% (Fig. 13). This effect must be much stronger in the stagnation point configuration. That result is essential with respect to the interpretation of the measured heat flux rates in high enthalpy facilities and flight experiments in similar environments.

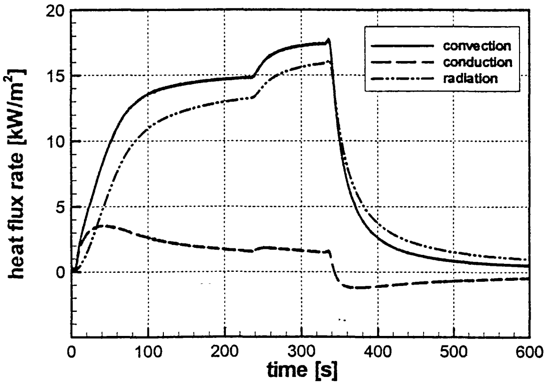

Figure 13. Heat flux rates for the tile sensor during the test at off-axis positions.

4.2.2 Measurement with HFM

For flat plate testing the HFM was integrated into the same holder, which had been used for the tile sensor. The main objective of the test, which was performed at FC I, was to check the influence of the arc heater radiation on the heat flux measurement with the HFM sensor. The HFM sensor was positioned at three off-axis positions (–20 mm, +20 mm and +50 mm). So, the increasing influence of the arc heater emission in dependency of the view angle of the surface could be demonstrated. The measured heat flux and temperature histories are given in Fig. 14. First, the sensor was positioned at -20 mm for the time interval between 13-17 s. No arc heater radiation could reach the sensor's surface at that position. After moving the sensor to +20 mm the heat flux rate increases by 20% (19-22 s). A further increase of the heat flux rate is observed at +50 mm (25-28 s), but this effect should only be interpreted qualitatively, since the slightly different flow condition there does not allow a quantitative comparison. In general, it seems that the influence of the arc heater radiation on the HFM heat flux measurement is stronger than on the tile sensor.

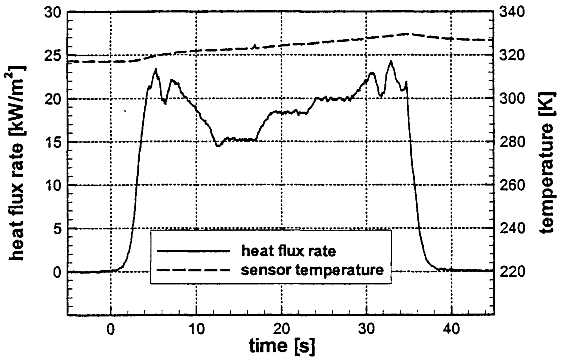

Figure 14. Heat flux rate and surface temperature measured with HFM during the test at off-axis positions.

A comparison of the heat fluxes measured with tile sensor and the microsensor (HFM) is given in the following table:

Table 3. Heat flux rates measured in the flat plate configuration at α = 0° at FC I.

	-20 mm		+20 mm	
Sensor	$\dot{q}_g$ [kW/m²]	T_s [K]	$\dot{q}_g$ [kW/m²]	T_s [K]
tile sensor	14.8±0.5	720	16.1±0.5	735
heat flux microsensor	15.3±0.5	324	18.3±0.6	327

Because of smaller differences in the surface temperatures of tile sensor and HFM sensor, the measured heat

© European Space Agency • Provided by the NASA Astrophysics Data System

flux rates are closer than the data of the stagnation point configuration. While for the tile sensor the arc heater radiation leads to a 9% increase in the heat flux rate (from 14.8 kW/m^2 to 16.1 kW/m^2), the radiation causes about 20% increase in the data of the microsensor. This result shows that the extraneous radiation like reservoir radiation, radiation from hot components of a space vehicle, etc. influences heat flux measurements with the microsensor in a stronger way than the tile sensor's data. Both sensors were calibrated using radiative calibration sources. For the HFM sensor it has to be checked, whether a radiative calibration source is sufficient for the measurement of convective heat fluxes.

5. CONCLUSIONS

Heat flux measurements were performed at re-entry flow conditions in the arc heated facility LBK using different heat flux sensors. The tests were carried out at two enthalpy levels in stagnation point as well as flat plate test configuration, in order to cover a broad range of heat flux rates and to study the influence of different gas composition and of extraneous radiation like arc heater emission.

The tile sensor was tested in a heat flux range of 15 to 245 kW/m^2 at surface temperatures up to 1500 K successfully. A maximum temperature drop of about 30 K was measured across its coating, which has a thickness of 300 µm. Comparative computations showed that the influence of the rear side boundary condition on the calculation of heat flux rates is negligible. So accurate data can be calculated from a surface temperature history measured with the thermocouple straight below the coating. In particular, all three surface heat flux rates, i.e. radiative, conductive and convective, were obtained in that way. The comparison of the measured and calculated data for different ambient pressure levels demonstrated the dependency of the tile material's thermal conductivity on the ambient pressure level.

It has been demonstrated that the heat flux microsensor (HFM) is applicable at heat flux rates up to 550 kW/m^2 in a high enthalpy flow field with high atomic oxygen concentration. Its very fast response time of 6 µs provides high resolution data, capturing strong heat flux gradients even across the free stream side shock. At the high enthalpy flow condition (FC II) the ratio of the heat flux rates measured with the HFM and tile sensors is significantly larger, which cannot be explained with radiation influence only. It seems that the HFM's Zynolyte layer has a higher surface catalycity compared to the black glass coating of the tile sensor.

The transient probe showed poorer repeatability than the other sensors. Its main advantage is the fact that it allows the measurement of heat flux profiles.

The tests in flat plate configuration showed that radiation from extraneous sources, like the arc heater, has more influence on the heat flux rates measured with the HFM sensor compared to the tile sensor. This phenomenon has to be considered in the evaluation of the heat flux data from high enthalpy facilities or areas of space vehicles, which are exposed to the radiation of other hot components. The validation of numerical codes with respect to heat flux determination should also consider this aspect.

ACKNOWLEDGEMENT

Part of this work was performed with the financial support of the German national technology program for future space transport vehicles TETRA.

REFERENCES

[1]Kindler, K., Ermittlung einer zeitlich veränderlichen Wärmebelastung auf einen endlichen Zylinder, 5. Jahrestagung der DGLR in Berlin, Vortrag Nr. 72, 1972.

[2]Hager, J. M., Langley, L. W., Ohishi, S., Diller, T. E., Microsensors for High Heat Flux Measurements, AIAA Journal of Thermophysics, vol. 7, no. 3, June 1992.

[3]Kawasaki Heavy Industries Ltd., Thermal Analysis of the Tile Heat Flux Sensor, KHI calibration thermal analysis document for DLR, January 2000.

[4]Gülhan, A., Esser, B., A Study on Heat Flux Measurements in High Enthalpy Flows, 35th AIAA Thermophysics Conference, AIAA-2001-3011, Anaheim, CA, June 2001.

[5]Gülhan, A., Arc Heated Facility LBK as a Tool to Study High Temperature Phenomena at Re-entry Conditions, DLR IB-39113-97A05, Oct. 1997.

[6]Bade, W. L., Yos, J. M., The NATA Code, Theory and Analysis, NASA CR-2547, 1975.

[7]Grisch, F., Bouchardy, P., Joly, V., Koch, U., Gülhan, A., Coherent Anti-Stokes Raman Scattering Measurements and Computational Modeling of Nonequilibrium Flow, AIAA Journal, vol. 38, no. 9, pp. 1669-1675, Sept. 2000.

[8]Koch, U., Gülhan, A., Esser, B., Grisch, F., Bouchardy, P., Rotational and Vibrational Temperature and Density Measurements by Planar Laser Induced NO-Fluorescence Spectroscopy in a Nonequilibrium High Enthalpy Flow, AGARD Conference on Advanced Aerodynamic Measurement Technology, Seattle, 1997.

[9]Gülhan, A., Esser, B, Koch, U., Experimental Investigation of Reentry Vehicle Aerothermodynamic Problems in Arc-Heated Facilities, AIAA Journal of Spacecraft and Rockets, vol. 38, no. 3, May-June 2001.

© European Space Agency • Provided by the NASA Astrophysics Data System

2002ESASP.487..689E

Session 7B

Shock Interactions/CFD Validation/Plume Flows

Chair: W. Schroeder & H. DeConinck

© European Space Agency • Provided by the NASA Astrophysics Data System

2002ESASP.487..689E

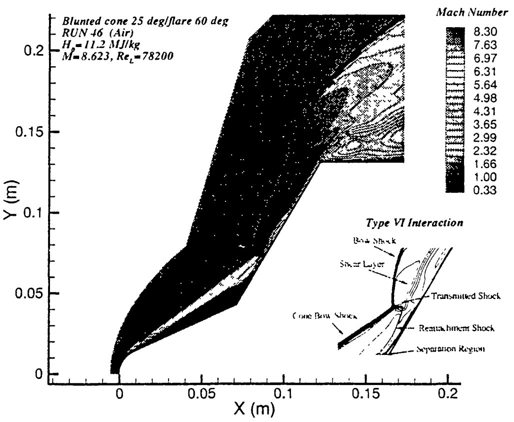

Figure 5: Mach number contours (Run 46).

Flow field analysis

The typical flow field structure is shown in Figs. 5, 6 and 7, respectively in terms of Mach number contours, streamlines and atomic oxygen mass fraction also zoomed in the nose and cone/flare junction regions. The numerical solutions of Run 42 (air, low enthalpy) and Run 46 (air, high enthalpy) on the finest grids are reported in the pictures. Due to bluntness a detached bow shock forms ahead of the hemi-spherical nose (see Fig. 6) whose strength is progressively weakened (up to the sphere-cone junction) due to the expansion waves originating from the nose, and the leading edge coincides with the stagnation point resulting in very high pressure and heat transfer. The shock wave/boundary layer interaction occurring around the cone-flare junction makes the flow to separate at the sphere-cone junction (the nose-tip) and to reattach towards the shoulder (trailing edge of the second cone), see Figs. 5 and 6. A multiple-vortex structure ($4\div5$ counter-rotating vortices) is predicted inside the separated area, and the bow shock is displaced upward due to flow deviation induced by separation. Figure 6 shows a different flow structure depending on Reynolds number and total enthalpy: in the case of Run 42 (high Reynolds number, low enthalpy) Fig. 6 (top) depicts a classical laminar shock wave/boundary layer interaction that yields a huge flow separation extending from the sphere/cone junction to the flare trailing edge (and that contains five unstable vortex structures); in the case of Run 46 (low Reynolds number, high enthalpy) Fig. 5 and 6 (bottom) show clearly clearly (see the enlargements) the shock/shock interaction occurring between the (cone) bow shock and the reattachment shock producing a resultant shock, a transmitted shock and a shear layer (interaction type VI of Edney's classification, solution with shock wave). The multiple-vortex structure is smashed down on the cone/flare model and flow reattachment is largely anticipated in this latter case. Figure 7 shows that a significant chemical dissociation is predicted around the model (at the cone nosetip and behind the transmitted shock) in the air free stream high enthalpy case (Run 46), with $Y(O)_{max} \simeq 0.22$ and $Y(NO)_{max} \simeq 0.09$, see also Fig. 8 where the mass fraction distributions along the stagnation line are reported (recall that the cone surface is non catalytic). Figure 8 also indicates that a negligible dissociation is predicted for the air low enthalpy test-case (Run 42), with $Y(O)_{max} \simeq 0.03$ and $Y(NO)_{max} \simeq 0.08$. Moreover, both pure nitrogen test cases behave as a perfect gas flow (mass fractions not shown, $Y(N)_{max} \simeq 0.035$ for the highest enthalpy test case, Run 45). The temperature distributions along the stagnation lines (Figs. 9 and

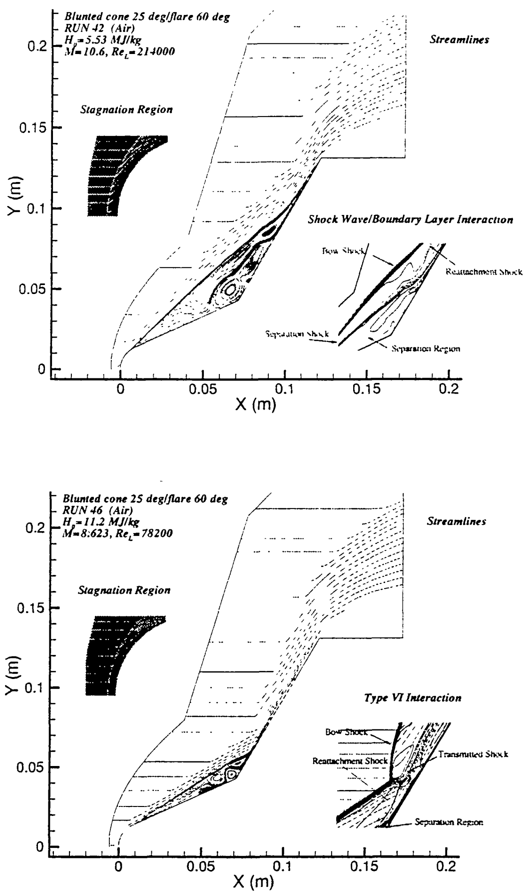

Figure 6: Streamlines for Run 42 (top) and Run 46 (bottom).

© European Space Agency • Provided by the NASA Astrophysics Data System